Journal of Materials Chemistry A

Mesopore-stimulated electromagnetic near-field: electrochemical synthesis of mesoporous copper films by micelle self-assembly

Journal:	*Journal of Materials Chemistry A*
Manuscript ID	TA-ART-06-2020-006228.R1
Article Type:	Paper
Date Submitted by the Author:	08-Sep-2020
Complete List of Authors:	Lim, Hyunsoo; University of Queensland, Australian Institute for Bioengineering and Nanotechnology (AIBN) Kim, Dabum; a. Department of Plant & Environmental New Resources, Kyung Hee University Kim, Yena; National Institute for Materials Science, WPI Center for MANA Nagaura, Tomota; University of Queensland, School of Chem Eng You, Jungmok; Kyung Hee University, Plant & Environmental New Resources Kim, Jeonghun; Kookmin University College of Science and Technology, Chemistry Kim, Hyun-Jong; Korea Institute of Industrial Technology, Surface Technology Center Na, Jongbeom; University of Queensland, Australian Institute for Bioengineering and Nanotechnology; National Institute for Materials Science, WPI-MANA Henzie, Joel; National Institute for Materials Science (NIMS), International Center for Materials Nanoarchitectonics (WPI-MANA) Yamauchi, Yusuke; University of Queensland, School of Chem Eng and AIBN

Mesopore-stimulated electromagnetic near-field: electrochemical synthesis of mesoporous copper films by micelle self-assembly

Hyunsoo Lim,[a] Dabum Kim,[b] Yena Kim,[c] Tomota Nagaura,[a] Jungmok You,[b] Jeonghun Kim,[d] Hyun-Jong Kim,[e] Jongbeom Na,[a,*] Joel Henzie,[c,*] and Yusuke Yamauchi[a,b,c,*]

[a] *Australian Institute for Bioengineering and Nanotechnology (AIBN) and School of Chemical Engineering, The University of Queensland, Brisbane, QLD, 4072, Australia.*

[b] *Department of Plant & Environmental New Resources, Kyung Hee University, 1732 Deogyeong-daero, Giheung-gu, Yongin-si, Gyeonggi-do 446-701, South Korea.*

[c] *International Center for Materials Nanoarchitechtonics (MANA), National Institute for Materials Science (NIMS), 1-1 Namiki, Tsukuba, Ibaraki 305-0044, Japan.*

[d] *Department of Chemistry, Kookmin University, 77 Jeongneung-ro, Seongbuk-gu, Seoul, 02707, Republic of Korea.*

[e] *Surface Technology Group, Korea Institute of Industrial Technology (KITECH), Incheon, 21999, Republic of Korea*

Keywords: Mesoporous Copper Film, Surface-Enhanced Raman Spectroscopy, Self-Assembled Micelles, One-Reaction Synthesis, Large SERS Substrate.

Abstract

Surface-enhanced Raman spectroscopy (SERS) is a powerful analytical method that uses localized surface plasmon resonances (LSPRs) to enhance the Raman cross-section of adsorbed molecules. Nanostructured copper (Cu) has been investigated as a SERS substrate in recent years because it is also a plasmon-supporting metal like gold (Au) and silver (Ag), but Cu is orders of magnitude more abundant in the Earth's crust. Although Cu is more prone to oxidation and tends to generate weaker LSPRs than Au or Ag, the sheer affordability of Cu metal drives demand for SERS applications where the highest levels of sensitivity are not necessary. In addition, simplifying the fabrication methods for SERS substrates and avoiding costly lithographical techniques is a problem to overcome. In this report, we describe a method to fabricate mesoporous Cu films (MCuFs) using self-assembled block copolymer micelles as pore-directing agents in an electrochemical deposition method. The pores generated by the micelles are relatively large (> 20 nm), which enables strong electromagnetic field enhancements *via* the LSPR. Different electrodeposition conditions such as potentials and times were tested to study MCuF formation and its effect of pore size and porous structure, and their effect on SERS activity. We found that the samples created with small micelles generated the most robust SERS response. Electromagnetic simulations indicate that small pores are important for generating strong fields, and that presence of interconnected grooves assists in the collection of light into these small pores. The optimal MCuF substrate generated an enhancement factor (EF) and limit of detection (LoD) of 3.8×10^{5} and 10^{-6} M, respectively. The results confirm that MCuFs are efficient for practical SERS applications due to the simple synthesis, high performance, and low cost.

Introduction

SERS is a non-destructive analytical technique to detect chemical species and obtain accurate molecular fingerprints for applications including pesticide detection,[1,2] bioanalytics,[3-5] and food safety analysis.[6] SERS substrates are composed of metal nanostructures that interact with visible light *via* collective oscillations of free electrons called surface plasmons (SPs). As SPs are launched across the surface of the metal, its accompanying electromagnetic (EM) field is concentrated at sharp edges, tips, and tiny sub-2nm gaps or discontinuities, forming local surface plasmon resonances (LSPRs). These so-called EM "hotspots" serve as antennae to enhance the Raman cross-section of nearby molecules many orders of magnitude.[7-10] The higher Raman cross-sections increase the analytical sensitivity of SERS hotspots, thus adding more hotspots per unit area/volume to a substrate should improve its overall sensitivity for molecular detection. The sensitivity of SERS substrates is typically calculated using the SERS enhancement factor (EF) method, which evaluates the enhanced Raman cross-section of a known number of molecules on the surface of a metal, versus a known number of molecules in solution. In addition, LoD method reports the lowest analyte concentration that is measurable with the substrate.[11]

SERS relies on substrates made of Au and Ag because these precious metals possess favorable bulk dielectric permittivities that enable large polarizations at optical frequencies.[12,13] In particular, Au is favored in SERS because it lacks a native oxide layer, allowing target molecules to sit on the surface of the metal where the EM field is strongest. Now scientists are searching for alternative plasmonic metals that may sacrifice some overall performance in SERS but deliver a much lower economic cost. Copper is an Earth-abundant metal with a commodity price in 2020 that is ~150-times cheaper than Ag and >10,000-times cheaper than Au.[14-16] These values fluctuate wildly because both Au and Ag have persisted as a form of financial asset outside of their applications in industry, whereas Cu is almost exclusively used as an industrial metal. Cu has interband transitions at 2.15 eV thus, it generates the highest EM enhancements above ~590-nm. Although oxidation is a concern with Cu surfaces, visible light irradiation of the LSPR has the propensity to reduce the native oxide layer of Cu nanoparticles to reveal the metal surface.[17] Various kinds of nanostructured Cu have been used as SERS substrates, including nanoparticles,[18-20] sharp spheroids,[21] and wires.[22] In the mesoporous field, porous Cu films fabricated *via* a dealloying method have generated good SERS enhancement factors.[23]

Porous films are interesting in the context of SERS because porosity affects the LSPRs, and the three-dimensional (3D) nature of porous films could enable a large number of EM hotspots per unit area/volume.

Generating ultrahigh surface area porous structures in metal films can be achieved with various methods that rely on dealloying, hard-templating, and soft-templating strategies. In particular, methods that rely on soft-templates have increased in popularity because self-assembled polymeric micelles are relatively rugged in electrochemical environments and can generate pores in various metals, including Au,[12,24,25] Cu,[26] platinum (Pt),[27] palladium (Pd),[28] rhodium (Rh),[29] nickel (Ni),[30] and their alloys.[31,32] The soft-templates can also be removed by soaking the substrate in the solvent. We previously demonstrated SERS sensing in electrochemically-generated mesoporous Au films.[12] These films can be generated in a one-step reaction, yielding a large surface area metal film containing a densely interconnected network of tips and gaps that present numerous hotspots for molecules to adsorb. These mesoporous Au films (MGFs) are also relatively insensitive to light polarization because of the semi-random distribution of pores in the surface and interior of the films, generating SERS EFs up to 1.2×10^5.[12] The SERS response of mesoporous Au nanoparticles (MGNPs) has also been reported.[12,25] Our group achieved the synthesis of MCuFs using self-assembled polymeric micelles and demonstrated its glucose-sensing application.[26] Despite the expectation of the MCuF to be an efficient SERS substrate, the study has not been reported yet. In this manuscript, we employed similar electrochemical deposition methods to generate mesoporous Cu films (MCuFs) for SERS to detect environmental pollution. Polystyrene-*block*-poly(ethylene oxide) (PS-*b*-PEO) block copolymer micelles were used as the pore-directing agent because it is rugged at various deposition potentials and the diameters of the resulting pores can be tuned by depositing micelles with different molecular weights. Rhodamine 6G (R6G) was used as an analyte which is a representative pollutant in water.[33] The best EF and LoD achieved with this method were 3.8×10^5 and 10^{-6} M, respectively. These electrochemical deposition tools are ubiquitous in most research institutes and do not require expensive setups such as high vacuum setups or lithography. Nor do they require a lot of steps and purification like colloidal synthesis/assembly methods. Furthermore, through this approach, high potential of application can be demonstrated in environmental areas such as water purification. We introduce an economic figure of merit (FOM, EF/price) for SERS substrates and explain why mesoporous Cu delivers an economic value at least 4-orders of magnitude higher than mesoporous Au.

Experimental section

Synthesis of MCuF.

***Preparation of the precursor*:** The precursor used to generate larger pores was prepared by dissolving 10 mg of PS_{63000}-*b*-PEO_{26000} (Polymer Source Inc.) in 3 ml of THF (99.9 %, Sigma-Aldrich *via* stirring at 300 rpm for 6-hours at 35 °C. Next, 1.5 ml of ethanol, 1.0 ml of 80 mM $CuSO_4$ aqueous solution, and 2.5 ml of 0.5 M H_2SO_4 aqueous solution were added in sequence to the solution and then stirred for another 4 hours to thoroughly mix the reagents. The precursor used to generate smaller pores was prepared with the same recipe, except that 7.5 mg of PS_{18000}-*b*-PEO_{7500} (Polymer Source Inc.) was added instead of the other block copolymer.

***Electrodeposition of MCuFs*:** An electrochemical workstation (CH Instruments, model 760E) was used to deposit the MCuFs in a three-electrode setup. Ag/AgCl served as the reference electrode, and platinum (Pt) wire served as the counter electrode. A 200-nm thick Au film sputtered on a *p*-doped Si wafer was used as the working electrode. All electrodeposition experiments were performed at room temperature without stirring the precursor solution. Residual micelles were removed from the surface and interior of the MCuFs by rinsing the samples in tetrahydrofuran (THF) and then soaking them in hot THF (40 °C). Then the MCuF samples were rinsed with deionized water (DIW) and dried under a stream of nitrogen gas (N_2).

***Reduction potential calculation*:**

$$Cu^{2+} + 2e^- \rightarrow Cu^0 + 0.34\ V$$

$$E_{red} = +0.34 - 0.197 - \frac{0.0592}{2}\ln[1] = 0.143\ V$$

where E_{red} is the electrochemical reduction potential (*vs.* Ag/AgCl) of Cu^{2+}, -0.197 V is the reference potential of an Ag/AgCl reference electrode, and pH of the solution is about 1 for this experiment. The reduction potentials of the MCuFs using PS_{63000}-*b*-PEO_{26000} and PS_{18000}-*b*-PEO_{7500} by the experiment are 0.05 V and -0.05 V, respectively. This is 0.09 V and 0.19 V lower than the calculated numbers. In the Cu precursor solution, Cu ions (Cu^{2+}) are making micelle-Cu ion bound formation. The bond needs much more energy to separate Cu ions from micelles.

Characterization.

Scanning electron microscopy (SEM)

Field emission scanning electron microscope (FE-SEM, JEOL JSM-7100F) with a hot electron gun was used for SEM observations. The MCuFs on silicon wafers were stuck on a metal SEM mount by using carbon tape and any additional metallic coating was not operated. The SEM observation condition was under vacuum less than 10^{-5} Pa with a 7-10 kV driving voltage.

Scanning transmission electron microscopy (STEM)

A focused ion beam (FIB) system (SII NanoTechnology Inc., Xvision200DB) with gallium (Ga) ion beam was used to prepare the nanometers thin lamellar MCuF sample. To protect MCuF from the Ga ion beam, micrometers thick carbon layer was deposited on the film before slicing it. The cross-section images and atomic structures of the MCuF were observed by using a STEM system (Hitachi HF5000) with a 200 kV accelerating voltage. Before the observation, the lamellar MCuF was cleaned by ozone plasma for 5 minutes to remove residual carbon impurities. The energy-dispersive X-ray spectroscopy (EDS) was also conducted in the same system without exposure in the air.

X-ray photoelectron spectroscopy (XPS)

Kratos Axis Ultra photoelectron (Kratos Analytical Ltd) system with mono Al Kα (1486.6 eV) x-rays was used for XPS. The MCuF on Si wafers was stuck on a metal XPS holder by using carbon tape. The spectroscopy was operated at room temperature. After the fast survey over the binding energy range from 0 eV to 1200 eV, each element was slowly scanned. Casa XPS (Casa Software Ltd) was used for the element and deconvolution analysis.

SERS measurement.

Preparation for SERS

95.8 mg of R6G (Sigma-Aldrich) was mixed with 2 ml of ethanol (DIW for the reference) to prepare 10^{-1} M R6G solution. Then, the solution was sonicated for 5 min to mix them completely. By diluting 10 times in ethanol, solutions with different R6G concentrations from 10^{-2} M to 10^{-7} M were prepared. As-deposited MCuFs were immersed in each solution for 30 minutes. The substrates in R6G solutions were taken out of the R6G solution and N_2 blowing was conducted to remove excessive R6G solution on MCuF surfaces. The

substrates were dried on a hot plate at 40 °C and used for SERS spectroscopy. The 40 °C temperature was sufficient to suppress the coffee ring effect and promote a more uniform distribution of analytes compared to samples dried at room temperature. The reference was confined in rubber with a hole (diameter: 6.35 mm; height: 1.64 mm) sandwiched by two quartz glass (thickness: 0.5 mm).

Enhancement factor formula

The Raman microscope and spectrometer (Renishaw) with a 785 nm excitation laser and 50x objective lens were used for the SERS studies on MCuFs. The laser intensity was calibrated by using a bare Si wafer at 520 cm^{-1} peak for every measurement. The EF factors for SERS were calculated using the following formula.

$$\mathrm{EF} = \frac{(I_{SERS}/N_{SERS})}{(I_{Ref}/N_{Ref})}$$

where I_{SERS} and I_{Ref} are Raman intensities of R6G, respectively. N_{SERS} and N_{Ref} are R6G concentrations at I_{SERS} and I_{Ref}, respectively. For the estimation of molecular numbers, N_{SERS} and N_{Ref}, see the supplementary note 1.

Results and discussions

Synthesis of MCuFs with different deposition conditions and characterization

Fig. 1 illustrates the electrodeposition process to make the MCuFs, in addition to the SERS measurement setup. To generate MCuFs with different pore sizes, we used two kinds of block copolymers with different molecular weights (*i.e.*, PS_{63000}-*b*-PEO_{26000}; Mw: 63,000-26,000 and PS_{18000}-*b*-PEO_{7500}; Mw: 18,000-7,500). The electrodeposition procedure was optimized by varying the potentials from -0.3 to -0.7 V (*vs.* Ag/AgCl) and deposition times from 100 to 1800 s. We noticed that the nanoarchitecture of the porous Cu network could be tuned in these conditions, and we evaluated the effect of these morphological changes on SERS sensing. TEM measurements show that Cu^{2+} ions had no noticeable impact on the size/shape of the spherical micelles (**Fig. S1**). Interestingly, TEM images of block copolymer micelles exposed to Cu^{2+} (**Fig. S1a**) were suffused with tiny Cu nanoparticles that were reduced by the TEM beam. This observation proves that the micelles strongly associate with Cu^{2+} (*i.e.*, PS-*b*-PEO-Cu^{2+}) and that each micelle has a large carrying capacity of Cu precursor. Applying a potential drives the PS-*b*-PEO-Cu^{2+} micelles to assemble on the surface of the Au/Si

working electrode, forming the MCuF (step (iv) in **Fig. 1**). The MCuF is then dried and used in the SERS measurements (steps (v)-(vi) in **Fig. 1**).

Linear sweep voltammetry (LSV) was initially used to assess the reduction potential of Cu^{2+} in the presence of PS_{63000}-*b*-PEO_{26000} micelles in an aqueous solvent mixture (**Fig. 2a**). Cu^{2+} has a peak reduction potential at -0.06 V (*vs.* Ag/AgCl) and then the current was almost constant between -0.2 V and -0.6 V. Hydrogen evolution begins at -0.65 V. **Fig. 2b-f** show SEM images of MCuFs deposited for 600 s using potentials spanning -0.3 V to -0.7 V. The MCuFs deposited at -0.5 V for 600 s have a well-interconnected network of tips and pores which are highly uniform over the entire surface of the Au/Si electrode (**Fig. 2d**). Besides, the mean pore size calculated from the pore distribution is 46.6 nm (**Fig. S2a**). Potential is important because potentials that are too high (*e.g.*, -0.3 V and -0.4 V) do not generate a fast enough reduction of Cu^{2+} ions to encapsulate the micelles and build the three-dimensional cage structure (**Fig. 2b-c**). Low potentials (*e.g.*, -0.6 V and -0.7 V) cause the Cu^{2+} to reduce too quickly, generating Cu aggregation and leading to worm-like mesoporous Cu structures (**Fig. 2e-f**). Therefore, the MCuF deposited at -0.5 V with clear pores/voids are considered as an appropriate structure to evaluate the pore effect on SERS and will be focused in this study.

Deposition time also plays an essential role in the morphology of the MCuFs. We deposited the PS_{63000}-*b*-PEO_{26000}-Cu^{2+} micelle solution on different Au/Si working electrodes using -0.5 V for 100 s to 1,800 s (**Fig. 3a-e**). Interestingly, the mesoporous structure appears in all deposition time conditions. As the electrodeposition time increases, mesoporous structures become very clear, and the pore sizes are almost identical with the micelle sizes shown in **Fig. 3a-c**. **Fig. 2** and **Fig. 3** confirm that potential determines MCuF structures, not deposition time. When the deposition time is longer than 600 s, the distortion of the mesoporous formation starts, leading to generating Cu aggregated particles with high surface roughness (**Fig. 3d-e**). **Fig. S3** and **S4** show the spatial distributions of the MCuFs with different deposition times that are 600 s and 1200 s, respectively. The MCuF at -0.5 V and 600 s deposition time shows highly uniform mesoporous structures over the substrate (**Fig. S3**), while the MCuF at -0.5 V and 1200 s shows minor differences at edges of the deposition area (**Fig. S4**). When micelles do not exist in the precursor solution (step (iii) in **Fig. 1**), the film seems like Cu bumps without pores, as shown in **Fig. 3f** at even the optimized condition (-0.5 V and 600 s).

MCuFs using micelles with different molecular weights (PS_{18000}-*b*-PEO_{7500}) generate pores in Cu with different diameters that will affect SERS enhancement. **Fig. 4** shows the LSV of the Cu precursor solution, including PS_{18000}-*b*-PEO_{7500} micelles and the SEM images of the MCuFs deposited at the different potentials from -0.3 V to -0.6 V for 600 s. This potential range is between the potential of the Cu^{2+} reduction peak (-0.2 V) and the potential where hydrogen evolution occurs (-0.7 V) (**Fig. 4a**). At high potentials such as -0.3 V and -0.4 V, the mesoporous structures are not completely formed (**Fig. 4b-c**). PS_{63000}-*b*-PEO_{26000} generates the same kind of features (**Fig. 2b-c**). The mesoporous Cu structure is clearly formed at -0.5 V, as shown in **Fig. 4d**. Using the same potential and deposition time (-0.5V; 600 s) with either PS_{63000}-*b*-PEO_{26000} or PS_{18000}-*b*-PEO_{7500} at -0.5 V results in mesoporous Cu, but with different pore sizes and gaps (**Fig. 2d; Fig. 4d)**. PS_{18000}-*b*-PEO_{7500} generates smaller pores, which is 21.9 nm in mean diameter, as shown in **Fig. S2b**, in Cu because the diameter of the micelle is smaller. Potentials around -0.6 V cause aggregation, resulting in bumps in the Cu film which are brighter in the SEM image because they are taller (**Fig. 4e**). The two kinds of micelles behave similarly under the same deposition conditions and generate mesoporous structures with the same morphology but different pore sizes. Therefore we used them to study the impact of pore size on plasmonic enhancement and SERS sensing.

X-ray photoelectron spectroscopy (XPS) and scanning transmission electron microscopy (STEM) were operated to characterize the local structure and composition of the MCuF generated at -0.5 V and 600 s (**Fig. 5**; **Fig. S5**). **Fig. S5** shows a survey of the XPS peaks for the MCuF on the Au/Si substrate. The sharp main peaks match Cu, and there does not appear to be serious contamination on the surface beside peaks from carbon (C; 284 eV) and oxygen (O; 528 eV). High-resolution XPS on the Cu 2*p* peaks shows that the top surface is somewhat oxidized with CuO and $Cu(OH)_2$ (**Fig. 5a**). Even though the MCuF was exposed in the air for a couple of weeks before the XPS analysis, oxidization was minor, indicating the oxidized layer is a couple nanometers thick. The oxidized Cu layer is very thin (a couple of nanometers) and the further oxidation barely occurs in weeks and months, maintaining a brown color (**Fig. S3a** and **S4a**). The oxide layer will affect SERS intensity because the molecule cannot adsorb directly to the surface where the electromagnetic field is strongest. But recent experimental work describing the distance-dependence of SERS indicates that enhancement is still very strong up to 2-nm away from a metal surface.[33] A focused ion beam (FIB) system

was used to take a cross-section of the MCuF (-0.5 V; 600 s) and examine it with STEM (**Fig. 5c-f**). **Fig. 5c-e** show this cross-section where mesopores are overlayed with an elemental map. A high-resolution STEM (HR-STEM) image of the MCuF in **Fig. 5f** shows that it has the characteristic *fcc*-structure of Cu but the film is polycrystalline.

The MCuFs demonstrated in **Fig. 2**, **3**, and **4** contain structures that act as hotspots such as tips with round surfaces and pores surrounded Cu, thus high SERS enhancement and sensitivity are expected. R6G is a fluorescent dye and has long served as a model compound to examine SERS enhancement.[10] The EF formula in the experimental section was used to calculate EF, whereas LoD is the lowest R6G concentration detected by the SERS substrates. The MCuFs using PS_{63000}-*b*-PEO_{26000} deposited at -0.5 V for 600 and 1200 s, which are named 'MCuF-1' and 'MCuF-2' in this report, were compared to study the roughness effect on the MCuFs for SERS sensing. This is because MCuF-1 is the optimized mesoporous structure and MCuF-2 has the similar structure, but different roughness, as shown in **Fig. 3c** and **3d**. In addition, they show a little difference of the EFs at 10^{-5} M R6G which may be from the roughness difference (**Fig. S6** and **S7**). The MCuF using PS_{18000}-*b*-PEO_{7500} deposited at -0.5 V for 600 s, which is named 'MCuF-3' (**Fig. 4d**), was compared to MCuF-1 to investigate the pore size effect for SERS sensing. As described above, using polymeric micelles with different molecular weights leads to different pore sizes, enabling the comparison of different pore sizes on SERS sensing. The cross-sections from 10^{-1} M R6G in aqueous solution which is confined in a column (diameter: 6.35 mm; height: 1.64 mm) were used as a reference. The experimental details are described in the experimental section.

Fig. 6a shows the Raman cross-sections of R6G with different concentrations on MCuFs-1. 10^{-1} M R6G in aqueous solution was used as a reference. The Raman intensity (counts per second) of R6G on the MCuFs at various concentrations (10^{-2}, 10^{-3}, 10^{-4}, and 10^{-5} M) was monitored at the main Raman peaks (1183, 1310, 1361, and 1508 cm^{-1}) and compared to the 10^{-1} M R6G reference (black line in **Fig. 6a**). The MCuF outperformed the reference sample under all conditions, showing that Cu enhances the local EM field for SERS analysis. The four peaks were observed up to 10^{-6} M R6G concentration, confirming that the LoD of MCuF-1 is 10^{-6} M. **Fig. 6d** plots the experimental EFs using the 1361 cm^{-1} peak of R6G. Interestingly, the

EFs increase as R6G concentration decreases, suggesting that higher concentrations create bulk-like films which dampen the SERS effect. The highest EF for the MCuFs was 8.5×10^4 at 10^{-6} M R6G.

Fig. 6b shows the Raman cross-sections of R6G with different concentrations on MCuFs-2. The same reference (10^{-1} M R6G in aqueous solution) was used in the earlier experiments. For the MCuFs-2, it also shows very sharp and higher SERS intensities at 10^{-2}, 10^{-3}, and 10^{-4} M R6G compared to the reference with 10^{-1} M R6G (black line in **Fig. 6b**). The EFs calculated by the 1361 cm^{-1} peak increase as the R6G concentrations decrease, as shown in **Fig. 6e**, matching the trend observed in **Fig. 6d**. The LoD using the MCuF-2, however, is 10^{-5} M R6G, while the LoD using the MCuF-1 is 10^{-6} M. The highest EF is 4.7×10^4, which is about half compared to that of MCuFs-1 (8.5×10^4).

To summary the effect of deposition potential and time, we calculated the pore areas on the surface of the MCuFs by using the monochromatic method (**Fig. S8** and **S9**). According to calculation, deposition time have an effect on the SERS response of the MCuFs. We sought to understand how the local structural features generated by the electrochemical conditions impacted SERS. Initially, we considered roughness generated by the different electrodeposition conditions. When comparing the two substrates with deposition times 600 s (MCuF-1) and 1200 s (MCuF-2) at 10^{-2} M R6G (**Fig. 6d** and **6e**), the MCuF-2 shows higher EF which is 3.7×10^3 than that of the MCuF-1 which is 6.5×10^2. As shown in the atomic force microscopy (AFM) results in **Fig. S7**, the root means square roughness (*Rq*) of the MCuF-1 and MCuF-2 are 10.8 nm and 16.4 nm, respectively. As the first report about the roughness effect on the SERS study was demonstrated,[35,36] increasing surface roughness of a substrate leads to higher SERS intensities due to a generated hierarchical structure leading to 3D gaps and tips that enhance the E-field as an LSPR in comparison with its flat counterpart. The number of exposed pores and the pore area on the film surface are not changed by the deposition time, thus it is not responsible for the difference in EF (**Fig. S8**). The EFs with the MCuF-1 and MCuF-2 at 10^{-5} M are 7.9×10^4 and 4.0×10^4 (**Fig. 5d, 5e,** and **Table S1**), respectively. And no SERS peak at 10^{-6} M is observed with the MCuF-2. We believe that low R6G concentration with low viscosity does not allow many R6G molecules to stay on the Cu surface by capillary effect.

To investigate the pore size effect, SERS studies were conducted by using the MCuFs-3 (**Fig. 4d**) and compared to the results of the MCuFs-1 (**Fig. 2d**). **Fig. 6c** shows the Raman cross-sections on the MCuFs-3

with different R6G concentrations. The 10^{-1} M R6G in aqueous solution was used as a reference. The MCuFs at entire R6G concentrations (10^{-2} M, 10^{-3} M, 10^{-4} M, 10^{-5} M, and 10^{-6} M) showed higher SERS intensities than that of the reference at 1361 cm^{-1} (**Fig. 6c**). This indicates the MCuF-3 is an effective substrate for SERS sensing. The pore size effect on the SERS is investigated by comparing the EFs in MCuF-1 (**Fig. 6d)** and MCuF-3 (**Fig. 6f**). In terms of the EFs, MCuFs-3 showed higher EFs than that of MCuFs-1 throughout the entire range of R6G concentrations. The highest EF of the MCuF-3 at 10^{-6} M (**Fig. 6f**) is 4.5-times higher compared to that in MCuF-1 (**Fig. 6d)**. Both MCuFs with different pore sizes showed the same LoD, which is 10^{-6} M. As shown in **Fig. S2**, the MCuF-3 has narrower pores between the Cu structures (**Fig. 4d**) than that of the MCuF-1 (**Fig. 2d**), but the interconnectivity of these tiny junctions may play a role in the SERS performance of MCuF-3. For comparison, flat Au and Cu films were also examined in SERS experiments using 10^{-5} M R6G and compared to MCuF-1, 2, and 3. The flat Au film generated a tiny amount of signal at around 1360 cm^{-1}, while the flat Cu film detected no peaks of R6G (**Fig. S10**). The experimental results are summarized in **Table S1** in the supplementary information.

Numerical modeling can help explain how morphology launches plasmon resonances on the surfaces of metal nanostructures, and the influence of local nanostructures in collecting and concentrating light in the near-field for SERS. The optical properties of the three primary film morphologies (MCuF-1, 2, and 3) were modeled using the finite difference time domain (FDTD) method. Initially, representative SEM images from each morphology were transformed into 50-nm thick, two-dimensional (2D) Cu films supported on the surface of a 200-nm thick Au film. Both Cu and Au were modeled using optical constants described by Palik.[37] Each film morphology was excited with a plane wave normal to the surface with the E-field polarized along one of three directions (θ = 0°, 45°, 90°). The near-field properties were collected 2-nm above the surface of the films, and the local electric field intensity (E^2) was plotted to show how the polarization of the E-field indicated by the green arrows influenced E^2. **Fig. 7a** shows the samples deposited for 600 s at -0.5 V using PS_{63000}-*b*-PEO_{26000} (MCuF-1). These deposition conditions generate relatively large pores (~50-nm) in the Cu film with some overlap. The 2D maps show that E^2 is the strongest at these overlapping metal junctions, especially when the polarization is perpendicular to the junctions. The average E^2 value for each map was computed and plotted versus wavelength in **Fig. S11a**. It shows that E^2 is largely insensitive to polarization, and that E^2 is the

strongest at ~640-nm. MCuFs deposited for 1200 s at -0.5 V using PS_{63000}-*b*-PEO_{26000} (*i.e.*, MCuF-2) generated slightly smaller pores (~40-nm) that were more numerous but with less junctions (**Fig. 7b**). The junctions that are present in the film seem to dominate the E^2 maps and exhibited a similar sensitivity to polarization as **Fig. 7a**. However, the average E^2 values have a bimodal distribution with peaks at ~610 and 650-nm (**Fig. S11b**). The absence of the 650-nm peak at $\theta = 45°$ indicates there is some preferential alignment of the micelles that may arise during the deposition. The Cu sample deposited for 600 s at -0.5 V using PS_{18000}-*b*-PEO_{7500} (MCuF-3) appeared to have smaller gaps, but they were closely spaced and formed long grooves in the metal (**Fig. 7c**). The E^2 maps are far more intense than the previous samples, and the strongest E^2 values appear in junctions that are perpendicular to the E-field. There are so many junctions in all directions that the average E^2 is roughly the same regardless of polarization. There also appears to be a bimodal distribution of LSPRs with peaks at 610 and 705-nm which is due to the multi-scale morphology of the pores. Overall, the average E^2 generated by the sample in **Fig. 7c** is ~3.8-times more intense than the other samples at their peak wavelengths. The stronger near-field intensity is due to the presence of more junctions, but the sample also has a higher percentage of pores per unit area versus the other samples (66% *vs.* 21% for **Fig. 7a** and 22% for **Fig. 7b**). Other researchers have noted that ultrasmall pores tend to generate strong LSPRs when a light can propagate deep into the pore.[33] But plasmon modes in grooves are confined by the walls of the grooves and may either propagate deeper into the gap (perpendicular to the film) or propagate along the groove (parallel to the surface of the film).[38] The MCuF-3 sample is superior because it combines the positive aspect of small pores with the good light collection properties of metal grooves and channels to generate the strongest SERS signals at the excitation wavelength.

Spectroscopists have found that only a tiny fraction of molecules on a SERS substrate contribute the vast majority of the SERS signal.[39, 40] The distribution of enhancements follows a power-law distribution—especially in the case of single-molecule SERS—where the highest EFs are skewed to the long tail of the distribution. Raman enhancement (η) can be roughly estimated using the fourth power rule $\eta_{max} = g^4$, where g is the local electric field (E).[41] The largest computed E^2 values for each sample at an excitation wavelength of 785 nm are 2.48×10^2, 2.62×10^2, and 2.84×10^3 for samples in **Fig. 7a**, **b,** and **c**, respectively, corresponding to an η_{max} of 6.15×10^4, 6.89×10^4, and 8.05×10^6. The simulated numbers follow the trend of the experimental

results. To analyze the long tail of the distribution, we performed a Weibull analysis on the simulated data in **Fig. 7a-c** because it represents a wide distribution of electromagnetic intensities. Other researchers have used a Weibull distribution to analyze experimentally-derived SERS EFs in self-assembled silver nanocube dimers.[42] The intensity data in each figure was arranged into a sorted list where the cumulative distribution function was calculated using all values greater than 1. Then the cumulative distribution was fit with a Weibull equation: $F(x) = 1 - \exp\{-(x/\beta)^{\gamma}\}$, where β is the scaling parameter indicating the average magnitude of the enhancement factor, and γ is the shape parameter which indicates the sensitivity of the enhancement factor to deviations from the ideal configuration. Details of the Weibull distribution are shown in **Figure S12**. The simulations corresponding to MCuF-1, MCuF-2, and MCuF-3 all had a shape parameter $\gamma < 1$, indicating that the distribution has a long tail. Most importantly, MCuF-3 had a scale parameter β ~10-times larger than MCuF-1 and MCuF-2, indicating that the average magnitude of enhancement factors in MCuF-3 was an order of magnitude larger than the other samples. This can be seen in the sorted list shown in **Figure S12,** where there are far more points in the higher end of the distribution of EFs.

Conclusion

In this report, we introduced MCuFs fabricated by one-step synthesis using electrodeposition for SERS applications. The mesoporous metal structure is effective as a plasmonic substrate and using the optimized MCuF enables practical use for SERS applications by reducing cost. The MCuFs with different deposition times (600 s and 1200 s) were compared, and the rough surface increased the SERS cross-section due to increased surface area and surface sharpness. However, thick MCuFs lead to the decrease of SERS intensities at low R6G concentration due to the lack of R6G on the surfaces. In terms of the pore size effect on SERS, MCuFs using PS_{18000}-*b*-PEO_{7500} have small pores which result in small gaps between Cu nanostructures. The film shows higher SERS intensity than the other MCuFs using PS_{63000}-*b*-PEO_{26000} throughout entire R6G concentrations. The maximum EF on the MCuF using PS_{18000}-*b*-PEO_{7500} is 4.5 times higher compared to the samples prepared using PS_{63000}-*b*-PEO_{26000} in the 10^{-6} M condition of R6G concentration. Numerical simulations indicate that the presence of small gaps and grooves in the PS_{18000}-*b*-PEO_{7500} generated sample (MCuF-3) were responsible for the strong enhancement factors. Weibull analysis of the simulated data showed

that all samples had a long tail distribution as expected in SERS substrates, but the EFs in MCuF-3 sample had a much larger average magnitude. In addition, this mesoporous structure is relatively insensitive to light polarization due to the intertwined structure of gaps and grooves in MCuF-3, which is beneficial for a practical device. This report indicates that mesoporous films should be designed and synthesized to obtain high roughness, thin film thickness, and narrow gaps that maximize SERS sensitivity. Furthermore, it is highly expected to apply to the environmental fields such as water treatment and pollutant detection, by using a high-performance SERS effect of the mesoporous copper film. Finally, Cu demonstrated that it can be an affordable and promising element that can commercialize SERS products by controlling the electromagnetic near-field.

Conflicts of interests

There are no conflicts to declare.

Acknowledgments

H.L. is supported by the University of Queensland (UQ) Research and Training Program. This research is supported by Korea Institute of Industrial Technology (KITECH). Y.Y. thanks the ERATO-FS "Yamauchi's materials space-tectonics project" supported by The Japan Science and Technology Agency (JST) for financial support. This work was supported in part by the World Premier International Research Center Initiate on Materials Nanoarchitectonics (WPI-MANA) from MEXT, Japan, and the Japan Society for the Promotion of Science (JSPS) Kakenhi Program (Grant Number: 20K05453). This work was performed in part at the Queensland node of the Australian National Fabrication Facility (ANFF-Q), a company established under the National Collaborative Research Infrastructure Strategy to provide nano- and micro-fabrication facilities for Australia's researchers. The authors acknowledge the facilities, and the scientific and technical assistance, of the Australian Microscopy & Microanalysis Research Facility at the Centre for Microscopy and Microanalysis, The University of Queensland.

References

1 D. Kim, Y. Ko, G. Kwon, U. J. Kim, J. H. Lee and J. You, *ACS Sustain. Chem. Eng.*, 2019, **7**, 15640-15647.

2 G. Kwon, J. Kim, D. Kim, Y. Ko, Y. Yamauchi and J. You, *Cellulose*, 2019**, 26**, 4935-4944.

3 J. Kneipp, H. Kneipp, K. Kneipp, *Chem. Soc. Rev.*, 2008, **37**, 1052-1060.

4 J. W. Kang, Y. S. Park, H. Chang, W. Lee, S. P. Singh, W. Choi, L. H. Galindo, R. R. Dasari, S. H. Nam, J. Park and P. T. C. So, *Sci. Adv.*, 2020, **6**, eaay5206.

5 B. Fazio, C. D'Andrea, A. Foti, E. Messina, A. Irrera, M. G. Donato, V. Villari, N. Micali, O. M. Maragò and P. G. Gucciardi, *Sci. Rep.*, 2016, **6**, 26952.

6 C. Andreou, R. Mirsafavi, M. Moskovits and C. D. Meinhart, *Analyst*, 2015, **140**, 5003-5005.

7 E. Hao and G. C. Schatz, *J. Chem. Phys.*, 2004, **120**, 357-366.

8 H. Metiu, *Prog. Surf. Sci.*, 1984, **17**, 153-320.

9 M. Rycenga, P. H. C. Camargo, W. Li, C. H. Moran and Y. Xia, *J. Phys. Chem. Lett.*, 2010, **1**, 696-703.

10 S. Nie, and S. R. Emory, *Science*, 1997, **275**, 1102-1106.

11 D. A. Armbruster and T. Pry, *Clin. Biochem. Rev.*, 2008, **29** Suppl. 1, S49-S52.

12 C. Li, Ö. Dag, T. D. Dao, T. Nagao, Y. Sakamoto, T. Kimura, O. Terasaki and Y. Yamauchi, *Nat. Commun.*, 2015, **6**, 6608.

13 H. Zhou, D. Yang, N. P. Ivleva, N. E. Mircescu, R. Niessner and C. Haisch, *Anal. Chem.*, 2014, **86**, 1525-1533.

14 D. Flanagan, Copper: U.S. Geological Survey Mineral Commodity Summaries, 52-53; January **2020**.

15 K. Sheaffer, Gold: U.S. Geological Survey Mineral Commodity Summaries, 70-71; January **2020**.

16 M. George, Silver: U.S. Geological Survey Mineral Commodity Summaries, 150-151; January **2020**.

17 A. Marimuthu, J. Zhang and S. Linic, *Science*, 2013, **339**, 1590-1593.

18 C. Kong, S. Sun, X. Zhang, X. Song and Z. Yang, *CrystEngComm*, 2013, **15**, 6136-6139.

19 Q. Shao, R. Que, M. Shao, L. Cheng and S. T. Lee, *Adv. Funct. Mater.*, 2012, **22**, 2067-2070.

20 M. Muniz-Miranda, C. Gellini and E. Giorgetti, *J. Phys. Chem. C*, 2011, **115**, 5021-5027.

21 X. Zhao, M. Deng, G. Rao, Y. Yan, C. Wu, Y. Jiao, A. Deng, C. Yan, J. Huang, S. Wu, W. Chen, T. Lei, P. Xu, W. He and J. Xiong, *Small*, 2018, **14**, 1802477.

22 D. Xu, Z. Dong, J. L. Sun, *Mater. Lett.*, 2013, **92**, 143-146.

23 L. Y. Chen, J. S. Yu, T. Fujita and M. W. Chen, *Adv. Funct. Mater.*, 2009, **19**, 1221-1226.

24 H. Lim, J. Kim, K. Kani, M. K. Masud, H. Park, M. Kim, S. M. Alsheri, T. Ahamad, N. Alhokbany, J. Na, V. Malgras, Y. Bando and Y. Yamauchi, *Small*, 2020**, 16**, 1902934.

25 H. Lim, T. Nagaura, M. Kim, K. Kani, J. Kim, Y. Bando, S. M. Alshehri, T. Ahamad, J. You, J. Na and Y. Yamauchi, *RSC Adv.*, 2020, **10**, 8309-8313.

26 C. Li, B. Jiang, Z. Wang, Y. Li, M. S. A. Hossain, J. H. Kim, T. Takei, J. Henzie, Ö. Dag, Y. Bando and Y. Yamauchi, *Angew. Chem. Int. Ed.*, 2016, **55**, 12746-12750.

27 H. Wang, L. Wang, T. Sato, Y. Sakamoto, S. Tominaka, K. Miyasaka, N. Miyamoto, Y. Nemoto, O. Terasaki and Y. Yamauchi, *Chem. Mater.*, 2012, **24**, 1591-1598.

28 M. Iqbal, C. Li, K. Wood, B. Jiang, T. Takei, Ö. Dag, D. Baba, A. S. Nugraha, T. Asahi, A. E. Whitten, M. S. A. Hossain, V. Malgras and Y. Yamauchi, *Chem. Mater.*, 2017, **29**, 6405-6413.

29 K. Kani, J. Kim, B. Jiang, M. S. A. Hossain, Y. Bando, J. Henzie and Y. Yamauchi, *Nanoscale*, 2019, **11**, 10581-10588.

30 D. Baba, J. Kim, J. Henzie, C. Li, B. Jiang, Ö. Dag, Y. Yamauchi and T. Asahi, *Chem. Commun.*, 2018, **54**, 10347-10350.

31 A. S. Nugraha, V. Malgras, M. Iqbal, B. Jiang, C. Li, Y. Bando, A. Alshehri, J. Kim, Y. Yamauchi and T. Asahi, *ACS Appl. Mater. Interfaces*, 2018, **10**, 23783-23791.

32 C. Li, H. Wang and Y. Yamauchi, *Chem. Eur. J.*, 2013, **19**, 2242-2246.

33 S. S. Masango, R. A. Hackler, N. Large, A. I. Henry, M. O. McAnally, G. C. Schatz, P. C. Stair and R. P. Van Duyne, *Nano Lett.*, 2016, **16**, 4251-4259.

34 C. Anderson and A. J. Bard, *J. Phys. Chem.*, 1995, **99**, 9882-9885.

35 M. Fleischmann, P. J. Hendra and A. J. McQuillan, *Chem. Phys. Lett.*, 1974, **26**, 163-166.

36 D. L. Jeanmaire and R. P. Van Duyne, *J. Electroanal. Chem.*, 1977, **84**, 1-20.

37 E. D. Palik, *Handbook of optical constants of solids*. Academic press: 1998; Vol. 3.

38 C. L. C. Smith, N. Stenger, A. Kristensen, N. A. Mortensen and S. I. Bozhevolnyi, *Nanoscale*, 2015, **7**, 9355-9386

38 Y. Fang, N. H. Seong and D. D. Dlott, *Science*, 2008, **321**, 388-392.

39 E. C. Le Ru, P. G. Etchegoin and M. Meyer, *J. Chem. Phys.*, 2006, **125**, 204701.

40 B. Pettinger, B. Ren, G. Picardi, R. Schuster and G. Ertl, *J. Raman Spectrosc.*, 2005, **36**, 541-550.

41 S. Y. Lee, L. Hung, G. S. Lang, J. E. Cornett, I. D. Mayergoyz and O. Rabin, *ACS Nano*, 2010, **4**, 5763-5772.

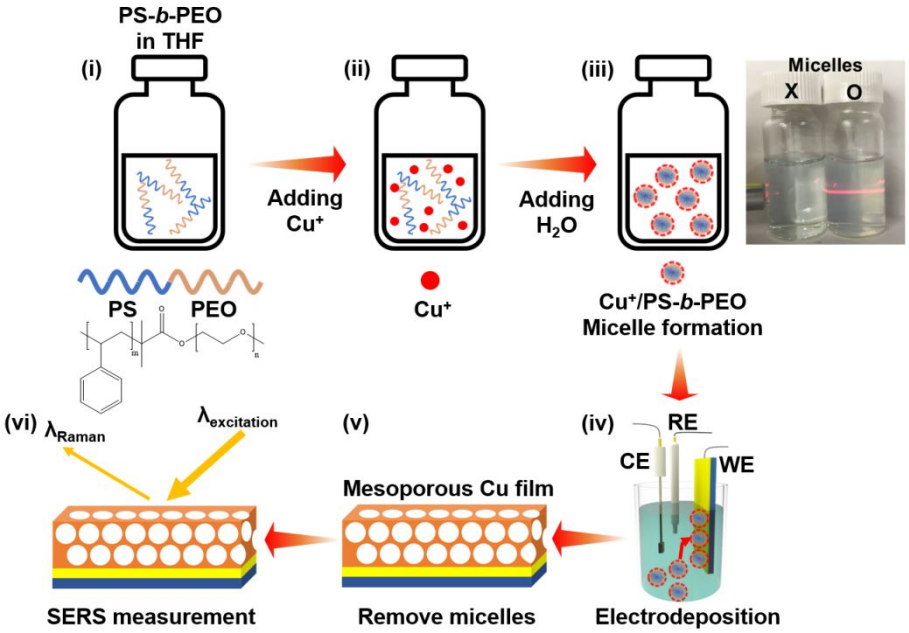

Fig. 1. The illustration of the MCuF fabrication process and its SERS application. The inset picture on the step (iii) shows Tyndall effect by self-assembled micelles in the Cu precursor solution.

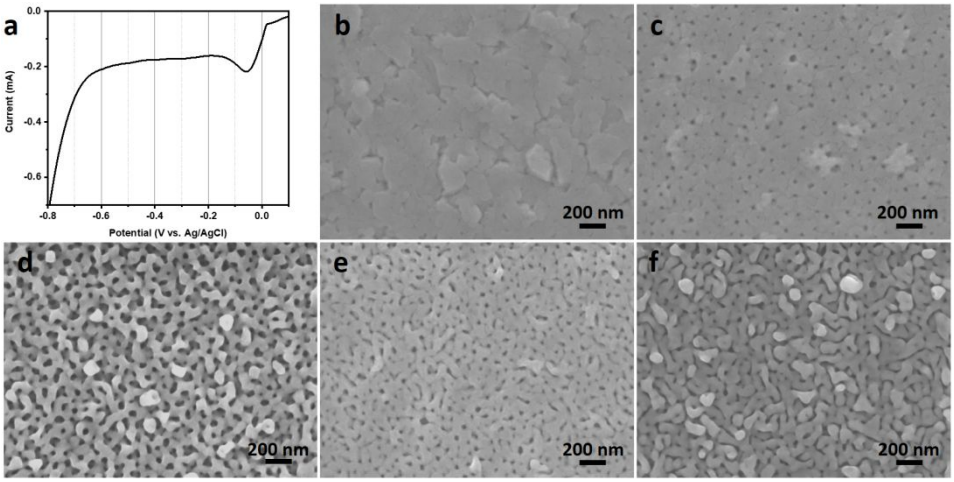

Fig. 2. (a) The LSV of the Cu precursor solution containing PS_{63000}-*b*-PEO_{26000} micelles. The SEM images of MCuFs using PS_{63000}-*b*-PEO_{26000} deposited at (b) -0.3 V, (c) -0.4 V, (d) -0.5 V, (e) -0.6 V, and (f) -0.7 V for 600 s.

458

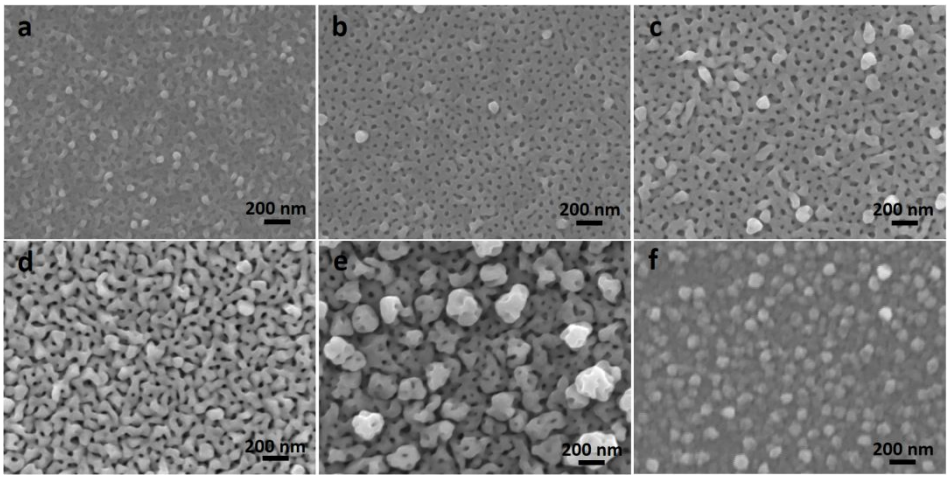

459 **Fig. 3**. The SEM images of MCuFs using PS_{63000}-*b*-PEO_{26000} deposited at -0.5 V for (a) 100 s, (b) 300 s, (c)
460 600 s, (d) 1200 s, and (e) 1800 s. (f) The SEM image of electrodeposited Cu film at -0.5 V for 600 s without
461 the micelles.

462

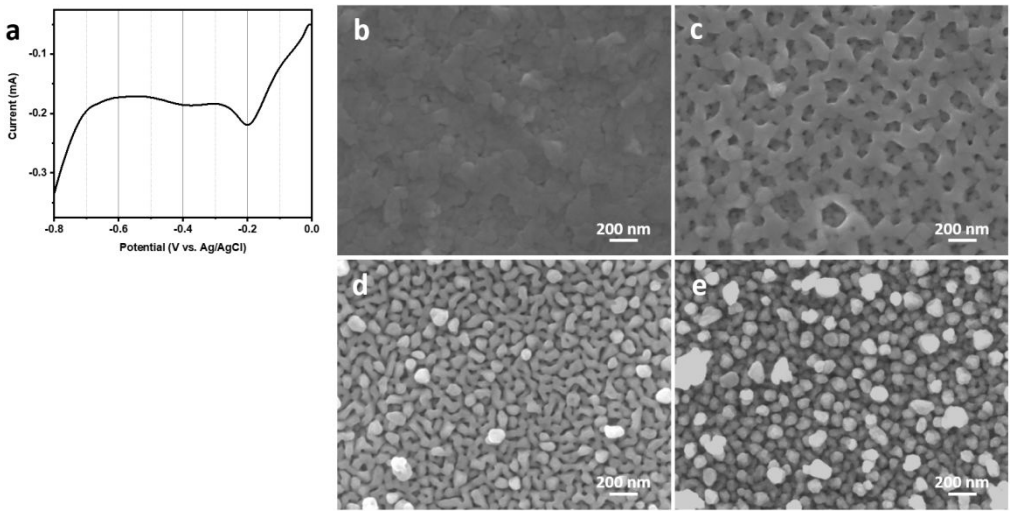

Fig. 4. (a) The LSV curve of the Cu precursor solution containing PS_{18000}-*b*-PEO_{7500} micelles. The SEM images of MCuFs using PS_{18000}-*b*-PEO_{7500} deposited at (b) -0.3 V, (c) -0.4 V, (d) -0.5 V, and (e) -0.6 V for 600 s.

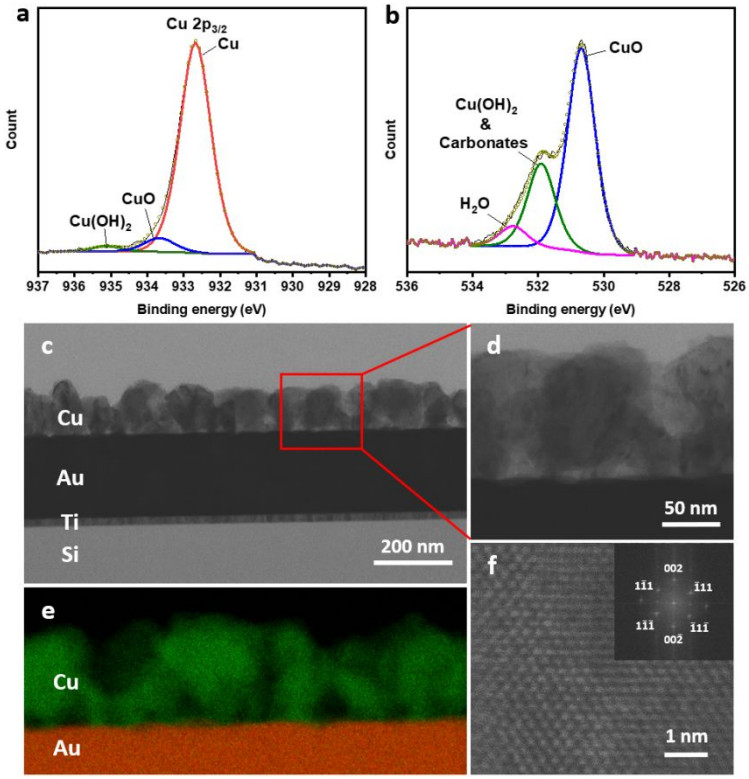

Fig. 5. (a,b) The XPS results of the MCuFs on the Au/Si substrate. (a) Cu 2*p* peaks deconvolution and (b) O 1*s* peaks deconvolution. (c-f) The STEM images of the MCuF on the Au/Si substrate. (c) Low- and (d) high-magnified STEM images of the MCuF and (e) its EDS elemental mapping. (f) The HR-STEM image of the MCuF and the *fcc*-crystal structure (inset).

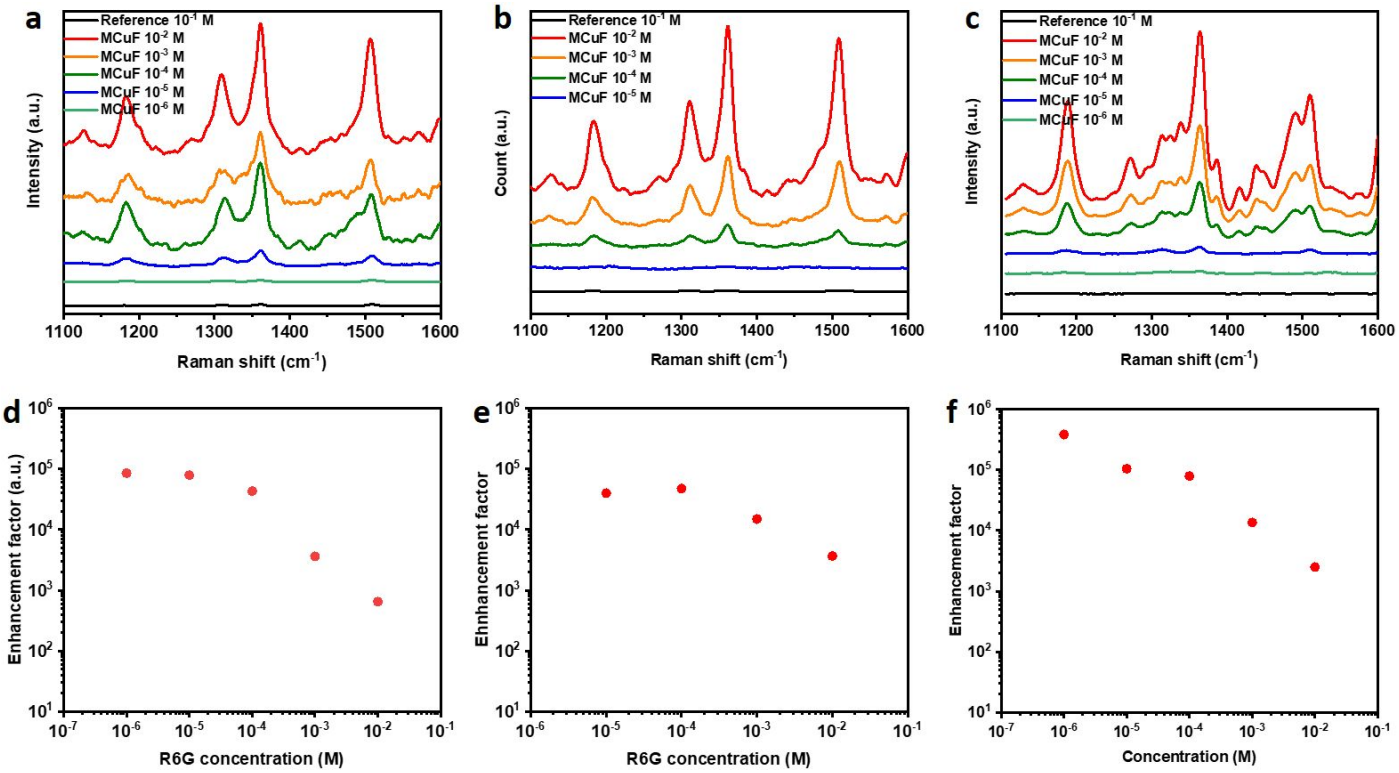

Fig. 6. (a) Raman cross-sections of R6G on a Si wafer (black line) and MCuFs using PS_{63000}-*b*-PEO_{26000} deposited at -0.5 V for 600 s (MCuF-1) and (b) 1200 s (MCuF-2) with various R6G concentration. (c) Raman cross-sections of R6G on a Si wafer (black line) and MCuFs using PS_{18000}-*b*-PEO_{7500} deposited at -0.5 V for 600 s (MCuF-3). (d-f) Enhancement factors versus R6G concentrations calculated by 1361 cm^{-1} peak plots regarding the results of **Fig. 6a-c**, respectively.

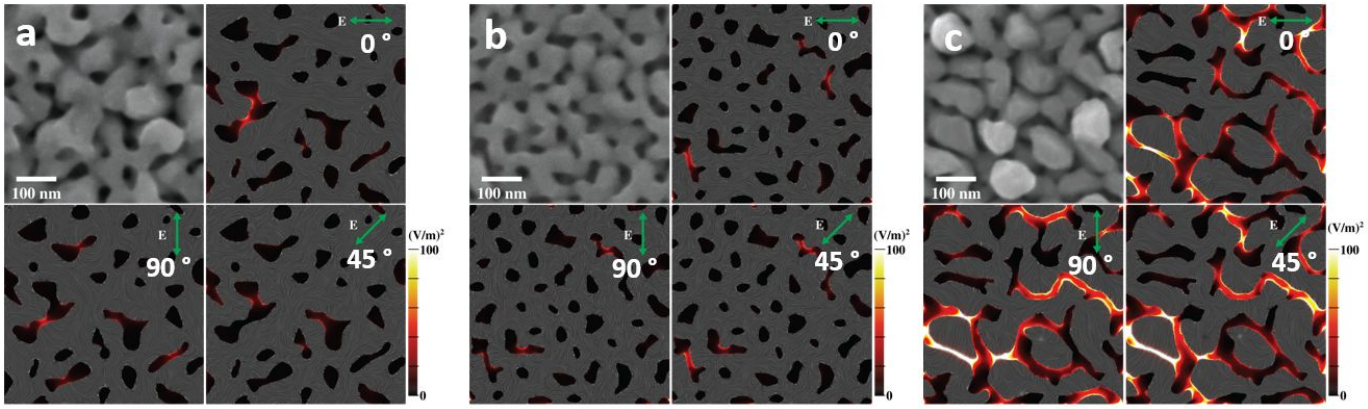

Fig. 7. The SEM images and optical simulations of MCuF using PS_{63000}-*b*-PEO_{26000} (a) at -0.5 V for 600 s (MCuF-1), (b) -0.5 V for 1200 s (MCuF-2), and (c) using PS_{18000}-*b*-PEO_{7500} at -0.5 V for 600 s (MCuF-3). The green arrows in **Fig. 7a-c** indicate the polarized E-field directions.